In situ validation of Tropical Rainfall Measuring Mission microwave sea surface temperatures

Chelle L. Gentemann, Frank J. Wentz, Carl A. Mears, and Deborah K. Smith
Remote Sensing Systems, Santa Rosa, California, USA

Received 13 August 2003; revised 5 November 2003; accepted 18 December 2003; published 21 April 2004.

[1] We present a validation study of sea surface temperature (SST) retrievals from the Tropical Rainfall Measuring Mission (TRMM) Microwave Imager (TMI). TMI SSTs are calculated using a radiative transfer-based retrieval algorithm, which precisely accounts for SST and wind effects on surface emissivity as well as atmospheric effects on brightness temperatures. TMI SSTs are compared to 4 years of the National Data Buoy Center, Tropical Atmosphere Ocean/Triangle Trans-Ocean Buoy Network (TAO/TRITON), and Pilot Research Moored Array in the Tropical Atlantic (PIRATA) moored buoy in situ SSTs. The microwave SSTs are shown to have a mean bias of $-0.07°C$ and a standard deviation of 0.57°C when compared to the TAO/TRITON and PIRATA SSTs. A discussion of time series and dependencies of the accuracy of the TMI SSTs in the presence of varying wind, cloud, and water vapor for each of the buoy arrays is presented. TRMM's precessing equatorial orbit allows the diurnal variability to be determined, revealing midafternoon warming of the surface layer at wind speeds less than 6 m s^{-1}. Low-wind TAO/TRITON collocations show diurnal warming in both the TMI and buoy retrievals, with TMI's diurnal peak larger and 1 hour before the buoy peak. This decoupling of the skin-bulk SSTs results in larger standard deviations for daytime low-wind situations. This result has direct implications for future in situ validation studies, in situ-based regression algorithms, and future blended infrared/microwave/in situ SST products. *INDEX TERMS:* 4594 Oceanography: Physical: Instruments and techniques; 4504 Oceanography: Physical: Air/sea interactions (0312); 4275 Oceanography: General: Remote sensing and electromagnetic processes (0689); 4227 Oceanography: General: Diurnal, seasonal, and annual cycles; *KEYWORDS:* microwave, SST, TRMM

Citation: Gentemann, C. L., F. J. Wentz, C. A. Mears, and D. K. Smith (2004), In situ validation of Tropical Rainfall Measuring Mission microwave sea surface temperatures, *J. Geophys. Res.*, *109*, C04021, doi:10.1029/2003JC002092.

1. Introduction

[2] The importance of measuring sea surface temperature (SST) is well established in both climate change research and operational forecasting. Monitoring long-term changes in the ocean temperature and circulation is important for understanding both the causes and results of climate change, since the oceans provide a net sink for both anthropogenic CO_2 emissions and the additional heat trapped by changes in the atmospheric composition, as well as providing an important SST-dependent feedback mechanism via evaporation.

[3] Interannual oscillations in SST, such as El Niño/La Niña, affect global-scale weather and fisheries productivity, with the attendant consequences for people and property. Each year, tropical cyclones threaten the lives and livelihood of coastal dwellers and cause millions of dollars in damages. Skillful forecasts of tropical cyclone intensity depend on timely, accurate measurements of the oceanic temperatures a given storm may encounter. Currently, infrared (IR) SSTs and buoys are the primary source for both operational and climate SST products.

[4] The buoy and IR SSTs are very useful, but suffer from several drawbacks. Buoy SSTs do not have the global coverage offered by satellite SSTs. The IR SSTs are widely acknowledged to have both spatial and temporal biases, including effects due to diurnal warming, water vapor attenuation, atmospheric aerosols, and incomplete removal of cloud contamination [*Emery et al.*, 1994; *Brown et al.*, 1985; *McClain*, 1989]. These errors can be partially mitigated through in situ-based corrections or sensor design but regional biases remain [*Reynolds et al.*, 1989]. Large uncertainties also occur in regions with persistent cloud cover that can block infrared retrieval of SST for weeks.

[5] In contrast to IR SSTs, microwave (MW) SSTs are unaffected by aerosols, and can be retrieved in the presence of clouds, simultaneous with wind speed, columnar water vapor, cloud water content, and rain rate [*Wentz et al.*, 2000; *Wentz*, 1998]. The cloud penetrating capabilities and insensitivity to aerosols properties allow MW SSTs to fill the gaps in the IR SST, and provide an important check for the presence of regional biases, especially in regions with sparse in situ measurements. MW SSTs are limited by

Copyright 2004 by the American Geophysical Union.
0148-0227/04/2003JC002092$09.00

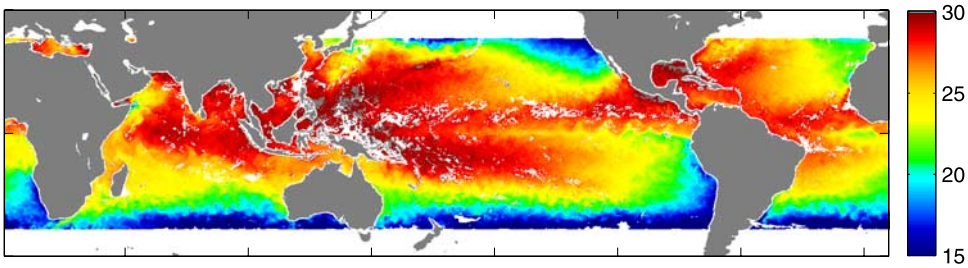

Figure 1. TRMM SST for 7–8 July 2000. Missing data are due to the presence of rain. TRMM's equatorial orbit limits retrieval to ±39° latitude.

errors such as decreased sensitivity at high wind speeds and by a relatively poor spatial resolution of 50 km.

[6] MW SST retrieval was first attempted using the SMMR instrument in 1979 [*Lipes et al.*, 1979; *Hofer et al.*, 1981]. Poor onboard calibration rendered the measurements too noisy for accurate SST retrieval. Subsequent MW imagers yielded much better radiometric accuracies but lacked the low-frequency channels needed for SST retrieval. Accurate retrieval of MW SSTs first became possible with the Tropical Rainfall Measuring Mission (TRMM).

2. Data

2.1. TMI Sensor Description

[7] TRMM was launched in November 1997, with an orbital inclination of 35° and an altitude of 350 km. This equatorial orbit yields coverage from 39°N to 39°S. Virtually complete Earth coverage is achieved by TMI in two days as shown by the 2-day average in Figure 1. Remaining white spaces are due to the presence of persistent rain.

[8] The TMI is a passive MW radiometer with nine linearly polarized channels measuring at 10.65, 19.35, 21.3, 37.0, and 85.5 GHz. Both vertical and horizontal polarizations are measured at all frequencies except 21.3 GHz, where only the vertical polarization is measured. The feed horns and main reflector rotate, with a period of 1.9 s, about an axis parallel to the local spacecraft nadir. The stationary hot reference absorber and cold calibration reflector are positioned so that they pass between the feed horns and main reflector once per scan. The temperature of the warm load is monitored by three thermistors, while the cold reflector views the cosmic MW background at 2.7 K. This frequent calibration minimizes receiver gain fluctuation contributions to the signal but does not correct radiometer nonlinearity (if it exists). At fairly regular intervals the platform yaws from forward (aft) viewing direction to aft (forward). Each scan consists of 104 discrete samples spaced by 8 km. The footprint of the 10.65 GHz channel is 45 km, which fixes the resolution of the SST product.

2.1.1. Calibration Problems

[9] The TMI instrument was carefully calibrated using SSM/I collocations, using the methodology described by *Wentz et al.* [2001]. A bias recognized in that paper has now been attributed to the degradation of the primary antenna. Atomic oxygen present at TMI's low altitude (350 km) led to rapid oxidization of the thin, vapor-deposited aluminum coating on the graphite primary antenna, resulting in a much higher antenna emissivity than expected. The measured radiation is comprised of the reflected earth scene and antenna emissions. Reflectivity of the antenna was deduced during the calibration procedure to be 96%. We have developed a correction algorithm, which utilizes additional information from instrument thermistors to estimate the antenna temperature, thereby reducing the effect of the temporal variance. Future radiometers are at higher altitudes and will not require this correction.

[10] To extend the mission length, in August 2001 the TRMM satellite was boosted from 350 km to an altitude of 402 km. Preboost, attitude of the satellite was determined by a horizon sensor, rendered obsolete at the higher altitude. Postboost attitude is determined using sixth-order Kalman filter of information from a magnotometer, gyroscopes, and a sun sensor. This methodology, while still estimating attitude within error specifications, has larger errors in determination of roll, pitch, and yaw than previously seen. Postboost, the increased errors in roll, pitch, and yaw immediately appeared in both the TRMM precipitation radar (PR) and TMI SSTs. The errors in satellite attitude resulted in increased errors in incidence angle calculation. Since the SST algorithm is extremely sensitive to incidence angle, the increased uncertainty in incidence angle caused pronounced biases in SST retrievals.

[11] A correction for these errors was developed and reprocessed TMI data were distributed as TMI V03. The error analysis was based on a comparison of TMI and Reynolds OI SST. We were very careful to try and correct only the orbital biases due to the attitude determination problem and not force TMI to match Reynolds. Our estimates of the roll error amplitude matched the GSFC PR estimated amplitude very closely.

2.1.2. Ocean Algorithm

[12] RSS has developed a physically based algorithm to retrieve SST [*Wentz*, 1998]. Using all TMI channels except those at 85.5 GHz, we simultaneously retrieve SST, wind speed, columnar water vapor, and columnar cloud water. SST retrieval relies primarily on the 10.7-GHz channel, with the other channels essentially providing corrections for the other geophysical variables. The algorithm was derived using the following procedure: representative model environmental scenes were generated by combining 42,195 radiosonde profiles, 5 cloud models, and a full range of values for SST, wind speed, and wind direction. Each scene is input to a radiative transfer model (RTM) to generate a simulated brightness temperature, T_b. The simulated T_b is then fitted to the known SSTs, wind, cloud, and rain, deriving linear regression coefficients that are applied to the corrected TMI T_bs.

[13] The 10.7-GHz T_b has a weak nonlinear response to SST and wind speed. Since the response is nearly linear, the small nonlinearities can be accounted for by a two-stage regression. 56 sets of algorithm coefficients are determined for different wind/SST regimes. A baseline algorithm produces a first-guess wind and SST, which are used to assign the observation on a specific wind/SST regime and identify the correct set of regression coefficients to use to produce a final SST.

[14] The main source of error in our retrieval algorithm is variation in the surface emissivity due to wind direction effects. We use the 10-m wind directions from the NCEP global analyses as an input to the algorithm to account for angular dependence of the emissivity; wind speed is calculated using the TMI T_bs. At wind speeds greater than 12 m s^{-1}, TMI SSTs have increased uncertainty. This is not a common problem: on average only 14% of winds in the region measured by TMI are greater than 12 m s^{-1}. SSTs are not retrieved when rain is present since scattering due to the large liquid droplets is difficult to model. Undetected rain on subpixel scales may cause a warm bias and can occasionally be seen as a warm ring around rain flagged data. These occasional errors can be removed by excluding data near raining pixels for climate quality SST products.

2.2. Buoy SST Data Set

[15] We have compiled a global buoy data set specifically for validation of MW products. The data set includes buoy retrievals from the National Data Buoy Center (NDBC), the Tropical Atmosphere Ocean/Triangle Trans-Ocean Buoy Network (TAO/TRITON), and the Pilot Research Moored Array in the Tropical Atlantic (PIRATA). Extensive error checking of all in situ measurements is used to exclude erroneous data. Buoys within 30 km of land are excluded from the data set.

[16] Many of the NDBC buoys are located quite close to land or in areas with high spatial/temporal variability. NDBC sensors have a resolution of 0.1°C and an accuracy of 1.0°C (www.ndbc.noaa.gov/rsa.shtml). Collocated SST measurements with these buoys can be expected to have significant biases and large random errors because of buoy location and relative inaccuracy. In contrast, TAO/TRITON and PIRATA moorings are located in the open ocean and have a stated accuracy of 0.01°C. Collocations with these buoys can be expected to have both lower biases and random errors.

[17] The TAO/TRITON and PIRATA hourly buoy SST data set is a mixture of 6-min averaged values returned once an hour from Autonomous Temperature Line Acquisition System (ATLAS) buoys and 10-min averages at the top of each hour (Next generation ATLAS). SST is measured at a depth of 1.0 m. NDBC buoys return an 8-min average once every hour, measured at a depth of 0.5–1.0 m. The hourly averaged 10-min SSTs from the TAO/TRITON and PIRATA arrays are only available once a year after mooring servicing but NDBC hourly data is available real-time from the Global Telecommunication System (GTS) reporting system. Postcalibration and error flagging of TAO/TRITON and PIRATA data is completed by the operating organization before the hourly buoy data is released, thus the hourly buoy data is thought to be more reliable and accurate.

2.3. Reynolds OI SST Data Set

[18] A second validation data set used in this study is the Reynolds Optimum Interpolated (OI) SSTs [*Reynolds and Smith*, 1994]. OI SSTs are a weekly blended IR satellite and buoy (both moored and drifting) product with 100-km resolution. The OI SSTs incorporate buoy measurements; therefore direct comparisons between the OI and buoys SSTs are not independent. OI SSTs will follow buoys very closely; differences may be due to small-scale SST variability and diurnal warming. Since OI SST is a weekly analysis, it does not resolve diurnal variability. It is included in the analysis so that diurnal excursions of the buoy and TMI SSTs may be examined.

3. Collocation Details and Complications

[19] Validation of satellite SST retrievals is complicated by several important differences between satellite and in situ measurements. First, it needs to be recognized that there is significant spatial/temporal inhomogeneity between in situ and satellite measurements. In situ measurements are time averages of SSTs at a single point, while satellite measurements are instantaneous measurements averaged over a large spatial footprint. Next, the measurements are taken at different depths: TMI is a measurement of the top millimeter of ocean while the in situ measurement is taken at 1-m depth.

[20] The upper ocean is usually well mixed and the 1-mm and 1-m measurements can be directly compared. Some differences between the measurements can be attributed to decoupling of the surface and 1-m SSTs. Satellite retrievals penetrate from a few microns (IR) to about 1 mm (MW). In situ sensors are typically located at a depth of 1 m. A thin cool "skin" layer of water, less than 1-mm thick, exists at the ocean surface. The vertical gradient in this thin layer is a function of the net ocean-atmosphere heat flux. Below this thin layer, during the daytime, low wind speeds and increased solar insolation can cause thermal stratification of the upper ocean, several meters thick [*Price et al.*, 1986; *Yokoyama et al.*, 1995]. The "bulk" water temperature is within this warm layer, but will peak slightly later in the day than the surface layer. Understanding the temporal variability and depth dependence of skin-bulk differences is important for accurate validation of SSTs between measurements at different depths. Recent publications have suggested that excluding daytime retrievals at wind speeds less than 6 m s^{-1} can minimize the diurnal effect [*Donlon et al.*, 2002], allowing more precise consideration of algorithm and instrument errors. This paper examines the diurnal variability measured by TMI and the buoy SSTs to directly address this suggestion.

[21] To examine the problems associated with comparing point measurements to 50-km averages, we examine individual buoy time series, which reveal considerable variability between moorings. Collocations generally agree, but specific differences and temporal and spatial patterns to mean differences and standard deviations are discussed.

[22] We then look at time series, averaging all data within the different arrays. This is another diagnostic tool for examining the validity of comparing the satellite skin and buoy 1-m temperatures. Since each of the buoy arrays have distinct geographic and therefore SST and water vapor

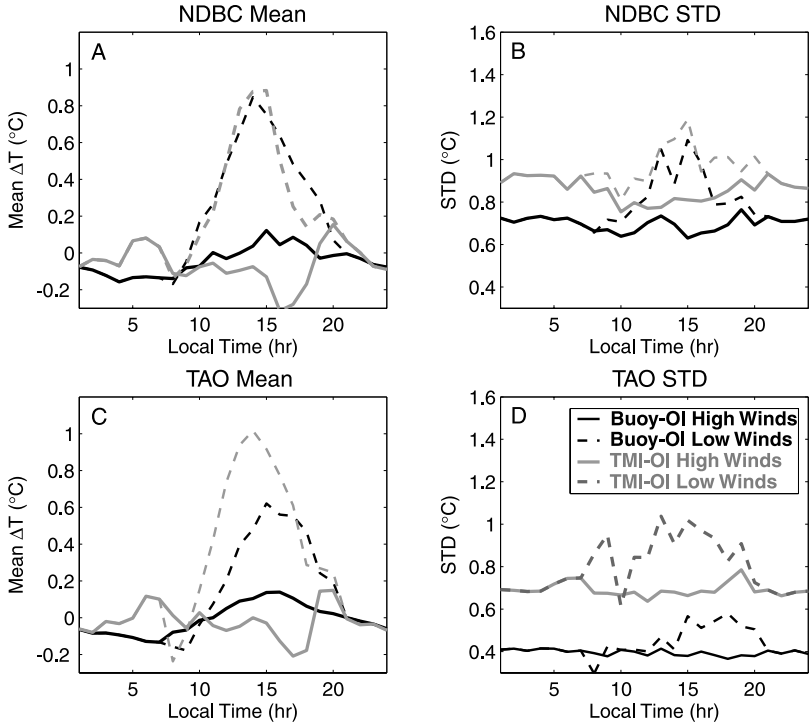

Figure 2. TMI and buoy diurnal cycle: mean difference and standard deviation. Reynolds OI SST is subtracted from both the buoy SST and TMI SST to provide an unbiased estimate of diurnal magnitudes. For both SSTs two cases are shown during the daytime: the solid line is for wind speeds between 6 and 10 m s^{-1}, and the dashed line is for wind speeds less than 3 m s^{-1}. For both data sets the mean difference and standard deviation is larger during the daytime for low wind speeds.

regimes, it is important to look at how each array compares with the other.

4. Results

4.1. Diurnal Variability

[23] The relationship between subskin and skin SST measurements was further examined by calculating the mean differences and standard deviations as a function of local time. In order to isolate diurnal variability, the low-frequency temporal and spatial contributions were removed from the TMI and buoy data sets by subtracting the collocated OI SSTs.

[24] Figures 2a–2d show the results for two cases: (1) only data with wind speeds between 6 and 10 m s^{-1} during the day, when enhanced vertical mixing in the upper ocean due to wind-induced mixing should stabilize the skin to subskin relationship, and (2) only data with wind speeds less than 3 m s^{-1}, when thermal stratification in the upper ocean layers will complicate the skin-bulk difference. The high-wind case is shown with solid lines while dashed lines indicate the low-wind case. In Figures 2a and 2c the high-wind and low-wind cases show two distinctly different relationships between TMI-OI ($\Delta T_{subskin}$) and buoy-OI (ΔT_{bulk}). At low wind speeds ΔT_{bulk} is decoupled from $\Delta T_{subskin}$: both figures show the $\Delta T_{subskin}$ diurnal peak as slightly larger than the ΔT_{bulk} peak. TAO/TRITON comparisons shown in Figure 2c show $\Delta T_{subskin}$ peaking 1 hour prior to the ΔT_{bulk} diurnal peak. At high wind speeds, both Figures 2a and 2c show a small diurnal peak in the buoy SSTs and a different diurnal variability in the TMI SSTs. The diurnal variability of the mean difference, at high winds, is likely residual error due to an imperfect correction for the oxidation of the primary antenna. The mean difference, including all buoy arrays, for wind speeds between 5 and 10 m s^{-1}, as a function of local time, is given in Table 1.

Table 1. TMI Minus Buoy SST Mean Difference as a Function of Local Time, Including Only Collocations With Buoy Wind Speed Between 5 and 10 m s^{-1}

Local Time, hour	Mean, °C
1	0.027
2	0.055
3	0.080
4	0.093
5	0.187
6	0.244
7	0.256
8	0.074
9	0.012
10	0.036
11	−0.034
12	−0.105
13	−0.118
14	−0.105
15	−0.183
16	−0.275
17	−0.310
18	−0.215
19	0.109
20	0.153
21	0.023
22	−0.014
23	0.009
24	0.001

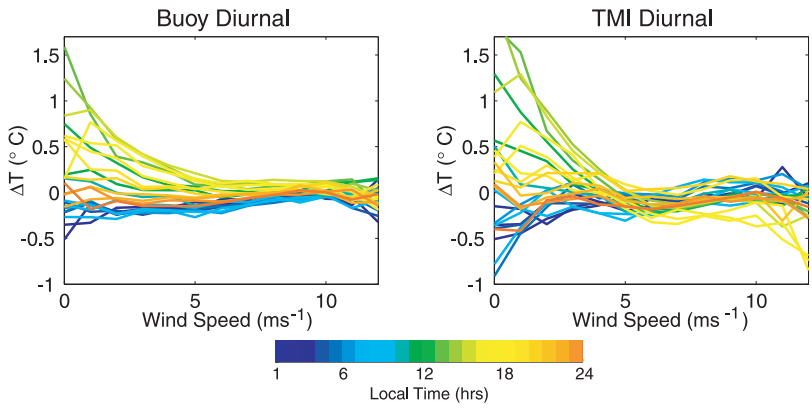

Figure 3. ΔT dependence on wind speed. Local time is indicated by the color of the line. TMI has a larger ΔT than the buoys. TMI and buoy daytime ΔT increases below 6 m s^{-1}. Daytime TMI values above 6 m s^{-1} are lower than nighttime values, while buoy daytime values above 6 m s^{-1} are higher than nighttime values. TMI nighttime values are fairly constant, decreasing at wind speeds less than 2 m s^{-1}.

The mean bias, −0.07°C, has been subtracted from the data in Table 1. Figures 2b and 2d show the standard deviations for each array. As expected, both residual standard deviations increase during daytime low-wind events, reflecting the increased variability due to diurnal warming.

[25] Figure 3 reveals the ΔT dependence on wind speed and local time. Each line represents a 1-hour average with daytime retrievals in green/yellow and nighttime retrievals in blue. During the daytime, ΔT is largest at low wind speeds, decreasing with increased wind speed until 6 m s^{-1}, above which the mean residual for both comparisons remains constant. ΔT_{bulk} is 0.95°C at 3 PM while $\Delta T_{subskin}$ is larger, 1.65°C at 2 PM. Both also show a small amount of cooling during the nighttime at wind speeds less than 1 m s^{-1} where wind driven convective overturning ceases and radiative cooling becomes the dominant mechanism. Interestingly, above 6 m s^{-1}, the $\Delta T_{subskin}$ daytime constant value is less than the $\Delta T_{subskin}$ nighttime constant while the reverse is true for the ΔT_{bulk} daytime/nighttime constant values.

[26] These results have specific significance for the regression-based algorithms used by AVHRR SSTs, especially the afternoon polar orbiters which drift from initial equatorial crossing times of 1:30 to crossing times of 5:30 or later over their lifespan. As advocated by *Donlon et al.* [2002], these results also emphasize the need for careful consideration of diurnal warming effects both during algorithm development and validation analysis. For the rest of our analysis, retrievals with wind speeds less than 6 m s^{-1} between 10 AM and 6 PM (local time) are excluded.

4.2. Rain Contamination

[27] The mean ΔT, TMI-in situ SST, and standard deviations are calculated from 3 years (1998–2000) of collocations to the TAO/TRITON, PIRATA, and NDBC buoy data set. As mentioned before, TMI SST is not retrieved in the presence of rain, but undetected subpixel rain can cause a warm bias in the SSTs, therefore several different rain flags accompany the orbital TMI SSTs. Mean error and standard deviations for ΔT, for the different rain filters, are shown in Tables 2a–2c. Gridded SST retrievals available at www.remss.com have had rain pixels and retrievals within 25 km of light rain removed. This filter assumes that light rain present in one pixel is likely in nearby pixels, but is small and may be missed by the rain algorithm. Another filter, excludes all retrievals within 25 km of any rain from the error analysis shown in Table 2b. This filter excludes more data than the mask used in Table 2a. It assumes that any rain calculated in a pixel is likely accompanied by rain in nearby pixels that may be undetected by the rain algorithm. The most conservative filter, shown in Table 2c, excludes all retrievals within 50 km of any rain. This filter excludes a large number of collocations.

[28] Occasional rain contaminated SSTs will produce a slight warm bias, warming the mean offset and increasing standard deviations as shown in Table 2a. Table 2a mean residuals calculated for TAO/TRITON (−0.16°C) and PIRATA (−0.07°C) and NDBC (0.15°C) are reasonably small. The standard deviations for the TAO/TRITON, PIRATA, and NDBC Table 2a collocations are 0.60°C, 0.56°C, and 0.79°C, respectively. Table 2b has slightly warmer mean biases, −0.08°C and 0.03°C for TAO/TRITON and PIRATA, and smaller standard deviations 0.57° and 0.55°C. NDBC has a larger mean bias (0.28°C) and standard deviation (0.92). The decrease in standard deviations for TAO/TRITON and PIRATA data is expected as the rain filter used in Table 2b excludes more rain-contaminated data. Table 2c has the lowest standard deviation (0.53° and 0.49°C for TAO/TRITON and PIRATA), agreeing well with the modeled algorithm accuracy of 0.50°C. While this filter has the least error, it excludes more data while not

Table 2a. Excluded TMI Retrievals Within 25 km of Light Rain

Buoy Array	Collocations	Mean	STD
TAO/TRITON	56116	−0.16	0.60
PIRATA	8634	−0.07	0.56
NDBC	33710	0.15	0.79

Table 2b. Excluded TMI Retrievals Within 25 km of Any Rain

Buoy Array	Collocations	Mean	STD
TAO/TRITON	28176	−0.08	0.57
PIRATA	4103	0.03	0.55
NDBC	19493	0.28	0.92

Table 2c. Excluded TMI Retrievals Within 50 km of Any Rain

Buoy Array	Collocations	Mean	STD
TAO/TRITON	6421	−0.13	0.53
PIRATA	929	0.02	0.49
NDBC	4984	0.25	0.90

appreciably decreasing the standard deviations. It appears for climate purposes that the 25 km/any rain flag (Table 2b) is sufficient, but the rain flags should be used to assign errors for assimilation into models. As expected, there are larger biases and standard deviations for the NDBC array. The larger standard deviations are likely due to the small-scale temporal and spatial variability common to the NDBC buoy locations while the warm bias appears to be due to increased side lobe contamination when near land. We have chosen to use the rain filter excluding all retrievals within 25 km of a raining pixel (2B) for the rest of the analysis.

[29] Notably, TMI does not include buoy measurements in the development of the retrieval algorithm, so accuracies estimated in this manner may be confidently extended globally, subject to the possible errors in the MW retrievals that were previously discussed. The statistics above were derived from hourly buoy data collocated with orbital single footprint TMI SSTs and are larger of than earlier published results by *Stammer et al.* [2003]. The previous study collocated weekly optimum interpolated TMI SSTs with TAO buoy and XBT data, this spatial and temporal averaging reduced random errors and thereby the STD is lower (0.46°C). The statistics derived in this paper are appropriate for the daily gridded data set distributed by RSS.

4.3. Individual Comparisons

[30] Evidence of small-scale SST variability for individual buoys is seen in the time series from four locations (Figures 4a–4f). The time series shown are collocated hourly buoy SST, orbital TMI SST, and the weekly OI SST. Daytime collocations with wind speeds less than 6 m s^{-1} and retrievals within 25 km of any rain were excluded. The buoy sites include PIRATA buoy 31001, TAO/TRITON buoy 32315, TAO/TRITON buoy 51017, and NDBC C-MAN station DRYF1, respectively. All time series show agreement over the 3-year period. TMI has some higher-frequency variability as compared to the buoy and OI SST time series (attributed to instrument noise, algorithm errors, and/or spatial/temporal mismatch). The OI SST is much smoother than either the buoy or TMI SSTs due to its weekly averaging. As expected, since the buoy SSTs are incorporated into the OI product, OI SSTs track the buoy SSTs very well, often obscuring the buoy SSTs in the figure. Variability at short timescales is missing from the OI SST but visible in both the TMI and buoy SSTs.

[31] Figure 4a shows data from a PIRATA buoy located in the western tropical Atlantic Ocean. This area has a very small annual cycle in SST, being generally coolest during June, when the South Equatorial Current is strongest. The

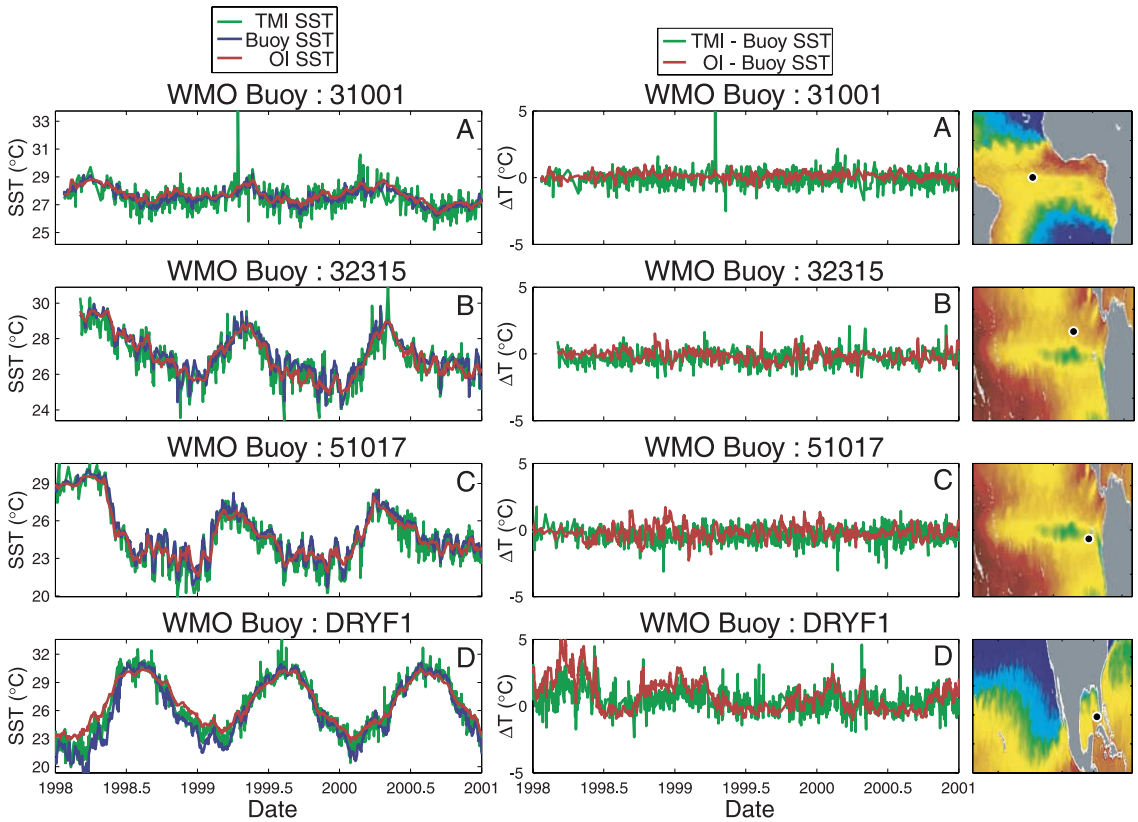

Figure 4. Time series of TMI, OI, and in situ SST for 1998–2001 corresponding to WMO buoys (a) 31001, (b) 32315, (c) 51017, and (d) CMAN station DRYF1: (right) time series of collocated retrievals of hourly buoy SSTs (blue), orbital TMI SSTs (green), and weekly averaged OI SSTs (red); (middle) the residuals, TMI-buoy SST (green), and OI-buoy SST (red), and (left) a map showing buoy location.

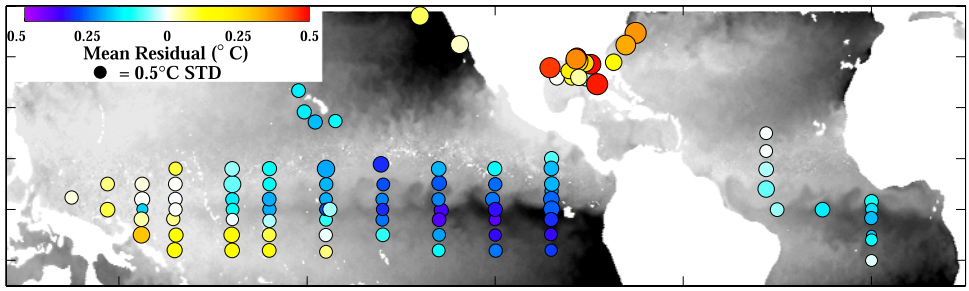

Figure 5. This image shows the buoy location, mean residual, TMI SST-buoy SST, and standard deviation of the residual for NDBC, PIRATA, and TAO/TRITON buoys. The mean residual is indicated by the color of the circle, while the standard deviation is indicated by the size of the circle. A typical weekly average SST is shown in the background. This figure is included to give the reader a feeling for the spatial distribution of the error statistics. The largest standard deviations are in the region of the Gulf Stream, a highly variable current.

buoy is located on the equator, just south of the Intertropical Convergence Zone (ITCZ), which contains substantial rainfall. The anomalous warm spike in the TMI retrieval in early 1999 is due to undetected rain contamination. We determined this by examining a map of the retrievals in that region. A rain cell was extremely close to the buoy location and nearby SST retrievals were all biased warm.

[32] Figure 4b shows results from a TAO/TRITON buoy, located north of the equatorial cold tongue. As expected, for this region with low temporal/spatial variability, both the OI and TMI SSTs are closely tracking the buoy SSTs. This buoy is located almost directly beneath the ITCZ and the warm bias seen in TMI on 30 March 2000 is due to rain contamination. This warm biased retrieval, and the one seen in Figure 4a, were both flagged as retrievals within 50 km of raining pixels. They are easily removed from the data set by simply removing data within 50 km of raining pixels, but this flag removes as much good data as bad. These questionable pixels have been left in the data set to allow researchers the freedom to choose between quantity or accuracy of retrievals.

[33] Figure 4c show results from another TAO/TRITON buoy, located on the southern edge of the South Equatorial Current. Tropical Instability Waves (TIWs) are present during the latter half of each year. These large-scale waves are easily detected with TMI [*Chelton et al.*, 2000; *Liu et al.*, 2000]. The TIWs are seen in all three data sets but the OI SST greatly underestimates their amplitude. Despite this buoy location in a tropical band of very high water vapor, the TMI SST algorithm is able to compensate for the columnar vapor content (which varies from 20 to 65.4 mm at the collocations), as demonstrated by its ability to track the buoy SST throughout the year.

[34] Figure 4d, results from Coastal-Marine Automated Network (C-MAN) station in the Gulf of Mexico, show both TMI and OI SSTs. Summer temperatures are in agreement, but both TMI and OI SSTs are underestimating 'cold' winter temperatures. The residuals clearly show both data sets with a warm bias that has a distinct annual cycle. In this region, during the winter the Loop Current is very visible in satellite imagery. It is highly variable in both time and space. During the summer, this current is still present but the temperatures in the Gulf are warmer, thereby, erasing the Loop Current's surface signature. The increased winter differences between the satellite and buoy measurements are likely due to this increased spatial variability.

[35] The mean differences and standard deviations for all individual buoys are shown in Figure 5. At each buoy location, the mean difference is indicated by color, while standard deviation is shown by circle diameter. This figure shows TMI SSTs as warmer than buoy SSTs in the Atlantic, but generally cooler than buoy temperatures in the Pacific. TAO/TRITON buoys near New Guinea all show warmer TMI retrievals. Many of the buoys in this region are close to nearby islands, resulting in a warm bias in TMI SSTs due to land contamination. NDBC

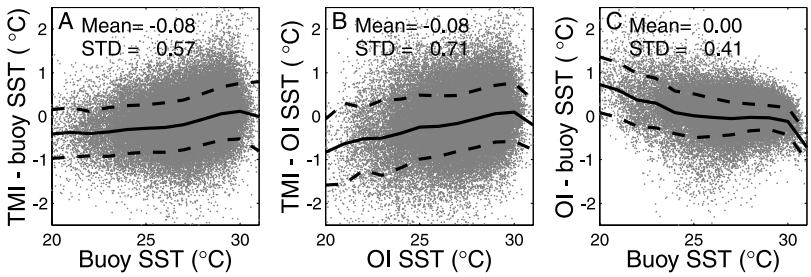

Figure 6. Comparisons between TMI, OI, and TAO/TRITON buoy SST for 1998–2001. (a) The residual, TMI-buoy SST, is plotted against the buoy SST. (b) TMI-OI SST is plotted against OI SST. (c) OI SST-buoy SST is plotted against buoy SST. In all three subplots the solid black line shows the mean residual for SST value, while the dashed lines are ± one standard deviation from the mean residual. The mean residual and standard deviation are shown in the upper half of each plot.

Table 3. TMI Minus Buoy Mean Difference and Standard Deviation as a Function of Buoy SST

Buoy SST, °C	Collocations	Mean, °C	STD, °C
20.0	172	−0.42	0.58
21.0	482	−0.38	0.57
22.0	1101	−0.4	0.5
23.0	1845	−0.37	0.54
24.0	3344	−0.3	0.55
25.0	4911	−0.27	0.55
26.0	7802	−0.26	0.56
27.0	10983	−0.19	0.57
28.0	12124	−0.07	0.59
29.0	9902	0.05	0.6
30.0	2906	0.11	0.62
31.0	131	0.00	0.72

buoys along the U.S. east coast have the largest standard deviations, likely because of the higher time-space variability in SSTs in that region.

4.4. Dependency of TMI SST on Environmental Variables

[36] Antenna temperatures measured at the satellite are a complicated mixture of surface emitted radiation, which is then absorbed/scattered through the atmosphere, and atmosphere emitted/reflected/scattered radiation. Our algorithm attempts to model the effect of cloud liquid water, columnar water vapor, and surface roughness on the retrieval. As mentioned before, anisotropic surface roughness effects are parameterized by wind speed, as calculated by TMI, and wind direction from the NCEP analysis model wind directions. The accuracy of this methodology is verified by examining the residual, ΔT (TMI - buoy SST), as a function of various environmental parameters. Only data from the TAO/TRITON array were included so as to have similar anemometer accuracy and heights.

[37] Figure 6 shows three residual biases: (A) TMI minus buoy SSTs, (B) TMI minus OI SSTs, and (C) OI minus buoy SSTs as a function of buoy or OI SST. In Figure 6a, there is a small cool bias (−0.14) and a slope to the mean residual indicating that TMI possibly has an error dependent on SST. Since we collocated OI SSTs with the buoy data set also, Figure 6b shows how TMI minus the OI SSTs depends on OI SSTs. The bias and slope are closely reproduced. A global comparison of TMI and OI SSTs does not show this bias or dependence on OI SST [*Stammer et al.*, 2003]. Finally, Figure 6c shows OI SST minus buoy SST as a function of buoy SST. Since buoy SSTs are used in the OI analysis it makes sense that the bias is 0.00°C and the standard deviation (0.41°C) is lower than the TMI/buoy or TMI/OI comparisons. This figure shows the OI SST having no bias and no dependence on SST above 25°C. Below 25°C the collocation data set shows a positive bias in the OI SSTs. This indicates that perhaps the cooler buoy SSTs are in a region (the equatorial cold tongue) or sampled in a manner where there is some biasing due to buoy/satellite spatial/temporal mismatch. The exact bias (TMI minus buoy SST) and standard deviation, as a function of buoy SST, are given in Table 3.

[38] Figure 7a shows ΔT plotted versus TMI cloud liquid water. Figure 7a demonstrates that we are able to retrieve SST through cloud, leaving no dependence in the SST on the cloud amount. Figure 7b plots ΔT versus TMI columnar water vapor. There is no apparent bias, reflecting the accuracy of the 21-GHz channel vapor retrieval and the algorithm's

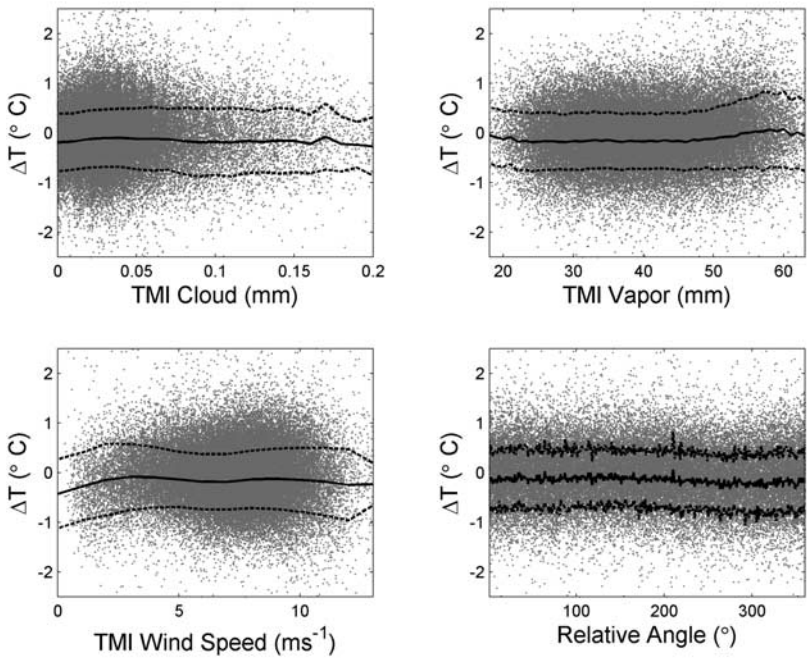

Figure 7. The residual TMI SST-TAO/TRITON and PIRATA buoy SST are plotted against (a) TMI cloud liquid water, (b) TMI columnar water vapor, (c) buoy wind speed, and (d) relative angle. The buoy wind speed is converted to a 10-m neutral stability wind. Relative angle is a measure of the angular difference between the satellite azimuth view angle and the wind direction vector. The black lines on each figure indicate the average residual, while the dashed lines are ± one standard deviation from the mean.

Table 4. TMI Minus Buoy Mean Difference and Standard Deviation as a Function of Buoy Wind Speed

Buoy wind speed (m s^{-1})	Collocations	Mean (°C)	STD (°C)
1	546	−0.28	0.68
2	1105	−0.15	0.72
3	1943	−0.09	0.66
4	2864	−0.09	0.61
5	4081	−0.14	0.56
6	7112	−0.18	0.56
7	10396	−0.19	0.56
8	9603	−0.14	0.58
9	6261	−0.13	0.61
10	2700	−0.15	0.64
11	690	−0.18	0.68
12	142	−0.25	0.72

ability to account for absorption of the 10.65-GHz channel, even at very high values of vapor (60 mm). The robustness of MW retrievals in the presence of water vapor and cloud should help parameterize errors in infrared SST fields.

[39] An anemometer set at a height of 4 m measures TAO/TRITON buoy wind speeds. In Figure 7c, a small dependence on the bias, as a function of wind speed exists. At wind speeds above 8 m s^{-1} there is a cool bias of 0.05°C in TMI. The bias and standard deviation as a function of wind speed is given in Table 4.

[40] In Figure 7d, ΔT is plotted as a function of relative angle. The relative angle is the angular difference between the satellite azimuthal look vector and wind direction vector as measured by the buoy. 180° indicates a situation where TMI is looking directly upwind, 0° directly downwind. The figure reveals a very small sinusoidal bias due to this effect. The bias is small and positive when TMI is looking near the same direction as the wind, and small and negative when TMI is looking the opposite. When corrected, the magnitude of the error is less than 0.1°C for high wind speeds. Uncorrected, the bias due to directional effects would be 3°C for wind speeds of 15 m s^{-1}.

5. Conclusion

[41] MW SSTs are of comparable accuracy and better coverage, but lower resolution than the currently available IR retrievals. The TMI SST have a −0.08°C bias and 0.57 standard deviation when compared to TAO and PIRATA buoys, while the AVHRR Pathfinder SST has a 0.02° and 0.53°C standard deviation [*Kilpatrick et al.*, 2001], when compared to in situ data. A recent study of daily SST availability from an IR polar orbiter, IR geostationary, and TMI gave SST coverage of 48%, 56%, and 78%, respectively [*Guan and Kawamura*, 2003]. The dramatic increase in coverage from the ability to measure SST through clouds and it's demonstrated accuracy, especially in high-water vapor regimes, should result in increased confidence and inclusion of MW SSTs in research efforts. This has already begun with studies of tropical instability waves [*Chelton et al.*, 2000; *Liu et al.*, 2000], and Rossby waves [*Stammer et al.*, 2003]. The observational errors in IR retrievals are different from the errors in the MW retrievals. Since both the MW and IR retrievals are of adequate temporal/spatial resolution and accuracy for utility in many climate research projects, investigations into biases that exist between these retrievals should result in improved algorithms and thereby improved accuracy for climate studies. Follow-on instruments including the AMSR series of instruments on AQUA (launched May 2003) and ADEOS-II (launched December 2003) will have an additional channel at 6.9 GHz, allowing even more accurate retrieval of SSTs. Additionally, both satellites are polar orbiters, yielding global SST retrievals. ADEOS-II will also carry SEAWINDS, a scatterometer, which will help to reduce SST errors by providing simultaneous wind speed and direction.

[42] **Acknowledgments.** This work was performed under NASA TRMM grant NAS5-00217 and JPL 1228578.

References

Brown, O. B., J. W. Brown, and R. H. Evans (1985), Calibration of advanced very high resolution radiometer infrared observations, *J. Geophys. Res.*, *90*, 1667–1677.

Chelton, D. B., F. J. Wentz, C. L. Gentemann, R. A. de Szoeke, and M. G. Schlax (2000), Microwave SST observations of transequatorial tropical instability waves, *Geophys. Res. Lett.*, *27*, 1239–1242.

Donlon, C. J., P. Minnett, C. L. Gentemann, I. J. Barton, B. Ward, J. Murray, and T. J. Nightingale (2002), Towards improved validation of satellite sea surface skin temperature measurements for climate research, *J. Clim.*, *15*, 353–369.

Emery, W. J., Y. Yu, G. A. Wick, P. Schluessel, and R. W. Reynolds (1994), Correcting infrared satellite estimates of sea surface temperature for atmospheric water vapor attenuation, *J. Geophys. Res.*, *99*, 5219–5236.

Guan, L., and H. Kawamura (2003), SST availabilities of satellite infrared and microwave measurements, *J. Oceanogr.*, *59*, 201–209.

Hofer, R., E. G. Njoku, and J. W. Waters (1981), Microwave radiometric measurements of sea surface temperature from the Seasat satellite: First results, *Science*, *212*, 1385–1387.

Kilpatrick, K. A., G. P. Podestá, and R. Evans (2001), Overview of the NOAA/NASA advanced very high resolution radiometer Pathfinder algorithm for sea surface temperature and associated mathchup database, *J. Geophys. Res.*, *106*, 9179–9197.

Lipes, R. G., R. L. Bernstein, V. J. Cardone, K. B. Datsaros, E. G. Njoku, A. L. Riley, D. B. Ross, C. T. Swift, and F. J. Wentz (1979), Seasat scanning multichannel microwave radiometer: Results of the Gulf of Alaska workshop, *Science*, *204*, 1415–1417.

Liu, W. T., X. Xie, P. S. Polito, S. Xie, and H. Hashizume (2000), Atmospheric manifestation of tropical instability wave observed by QuikSCAT and Tropical Rain Measuring Mission, *Geophys. Res. Lett.*, *27*, 2545–2548.

McClain, E. P. (1989), Global sea surface temperatures and cloud clearing for aerosol optical depth estimates, *Int. J. Remote Sens.*, *10*, 763–769.

Price, J. F., R. A. Weller, and R. Pinkel (1986), Diurnal cycling: Observations and models of the upper ocean response to diurnal heating cooling, and wind mixing, *J. Geophys. Res.*, *91*, 8411–8427.

Reynolds, R. W., and T. M. Smith (1994), Improved global sea surface temperature analyses using optimum interpolation, *J. Clim.*, *7*, 929–948.

Reynolds, R. W., C. K. Folland, and D. E. Parker (1989), Biases in satellite-derived sea surface temperature data, *Nature*, *341*, 728–731.

Stammer, D., F. J. Wentz, and C. L. Gentemann (2003), Validation of new microwave SST for climate purposes, *J. Clim.*, *16*, 73–87.

Wentz, F. J. (1998), Algorithm theoretical basis document: AMSR ocean algorithm, *RSS Tech. Rep. 050198*, Remote Sens. Syst., Santa Rosa, Calif.

Wentz, F. J., C. L. Gentemann, D. K. Smith, and D. B. Chelton (2000), Satellite measurements of sea-surface temperature through clouds, *Science*, *288*, 847–850.

Wentz, F. J., P. D. Ashcroft, and C. L. Gentemann (2001), Post-launch calibration of the TMI microwave radiometer, *IEEE Trans. Geosci. Remote Sens.*, *39*, 22–415.

Yokoyama, R., S. Tanba, and T. Souma (1995), Sea surface effects on the sea surface temperature estimation by remote sensing, *Int. J. Remote Sens.*, *16*, 227–238.

C. L. Gentemann, C. A. Mears, D. K. Smith, and F. J. Wentz, Remote Sensing Systems, 438 First Street, Suite 200, Santa Rosa, CA 95401, USA. (gentemann@remss.com)